Assessing the Ubiquity of Bloch Domain Walls in Ferroelectric Lead Titanate Superlattices

Edoardo Zatterin,[1,*] Petr Ondrejkovic,[2,*] Louis Bastogne,[3,*] Céline Lichtensteiger,[4] Ludovica Tovaglieri,[4] Daniel A. Chaney,[1] Alireza Sasani,[3] Tobias Schülli,[1] Alexei Bosak,[1] Steven Leake,[1] Pavlo Zubko,[5,6] Philippe Ghosez,[3] Jirka Hlinka,[2] Jean-Marc Triscone,[4] and Marios Hadjimichael[4,7,†]

[1]*ESRF—The European Synchrotron, 71 Avenue des Martyrs, 38000 Grenoble, France*
[2]*Institute of Physics of the Czech Academy of Sciences, Na Slovance 2, 18221 Praha 8, Czech Republic*
[3]*Theoretical Materials Physics, Q-MAT, Université de Liège, Allée du 6 août, 19, B-4000 Sart Tilman, Belgium*
[4]*Department of Quantum Matter Physics, University of Geneva, 24 Quai Ernest-Ansermet, 1211 Geneva, Switzerland*
[5]*Department of Physics and Astronomy, University College London, Gower Street, London WC1E 6BT, United Kingdom*
[6]*London Centre for Nanotechnology, 17-19 Gordon Street, London WC1H 0AH, United Kingdom*
[7]*Department of Physics, University of Warwick, Coventry CV4 7AL, United Kingdom*

(Received 26 March 2024; revised 5 September 2024; accepted 11 October 2024; published 26 November 2024)

The observation of unexpected polarization textures such as vortices, skyrmions, and merons in various oxide heterostructures has challenged the widely accepted picture of ferroelectric domain walls as being Ising-like. Bloch components in the 180° domain walls of $PbTiO_3$ have recently been reported in $PbTiO_3/SrTiO_3$ superlattices and linked to domain wall chirality. While this opens exciting perspectives, the ubiquity of this Bloch component remains to be further explored. In this work, we present a comprehensive investigation of domain walls in $PbTiO_3/SrTiO_3$ superlattices, involving a combination of first- and second-principles calculations, phase-field simulations, diffuse scattering calculations, and synchrotron-based diffuse x-ray scattering. Our theoretical calculations highlight that the previously predicted Bloch polarization in the 180° domain walls in $PbTiO_3/SrTiO_3$ superlattices might be more sensitive to the boundary conditions than initially thought and is not always expected to appear. Employing diffuse scattering calculations for larger systems, we develop a method to probe the complex structure of domain walls in these superlattices via diffuse x-ray scattering measurements. Through this approach, we investigate depolarization-driven ferroelectric polarization rotation at the domain walls. Our experimental findings, consistent with our theoretical predictions for realistic domain periods, do not reveal any signatures of a Bloch component in the centers of the 180° domain walls of $PbTiO_3/SrTiO_3$ superlattices, suggesting that the precise nature of domain walls in the ultrathin $PbTiO_3$ layers is more intricate than previously thought and deserves further attention.

DOI: 10.1103/PhysRevX.14.041052

Subject Areas: Condensed Matter Physics, Materials Science

I. INTRODUCTION

The large strain-polarization coupling intrinsic to ferroelectricity had historically led researchers to believe that rotations of the spontaneous polarization away from the polar axis, which could reduce the depolarization field energy, were forbidden [1]. In the past two decades, however, both theoretical predictions [2,3] and experimental studies using aberration-corrected transmission electron microscopy [4,5] have demonstrated that such rotations are in fact possible. This realization motivated a search for unconventional polarization arrangements in ferroelectric thin films and multilayers using scanning transmission electron microscopy (STEM), leading to the observation of a cornucopia of such arrangements, including ordered flux-closure domains [6,7], polar skyrmions [8], polar merons [9], and two-dimensionally ordered incommensurate structures [10].

Combined with predictions of non-Ising character at 180° domain walls [11,12], these findings have suggested

*These authors contributed equally to this work.
†Contact author: marios.hadjimichael@warwick.ac.uk

the possibility of ferroelectric domain walls acting as distinct two-dimensional entities with their own phase transitions and switchable polarization [13]. Recent work using 4D STEM and resonant soft x-ray diffraction reported the observation of Bloch components at 180° domain walls of $PbTiO_3$ and has highlighted how this would additionally result in domain wall chirality [8], both of which are now considered ubiquitous. However, only limited experimental evidence of such polarization components exists so far, due to the challenges in experimentally probing ferroelectric domain walls associated with their nanoscale nature. Furthermore, other works using different experimental techniques, including second harmonic generation, question this picture of chiral walls in $PbTiO_3$-based films [14,15].

In this work, we address the nature of 180° ferroelectric domain walls in ultrathin $PbTiO_3$ layers using a combination of state-of-the-art experimental and theoretical techniques. We employ first- and second-principles calculations within the generalized gradient approximation to simulate both bulk $PbTiO_3$ and $PbTiO_3/SrTiO_3$ superlattices. For bulk $PbTiO_3$, we confirm the previous predictions of Bloch components at 180° domain walls. For $PbTiO_3/SrTiO_3$ superlattices, on the other hand, we find that the Bloch polarization is extremely sensitive to the domain period of the ferroelectric layer and could disappear completely for domain periods energetically favored in realistic superlattices. In addition, and in contrast to predictions for bulk $PbTiO_3$, we find the Bloch polarization in the $PbTiO_3/SrTiO_3$ system to be extremely sensitive to the magnitude of epitaxial strain imposed.

Utilizing a combination of phase-field simulations, diffuse scattering calculations, and diffuse x-ray scattering measurements, we develop a method to detect and distinguish between nanoscale Bloch and depolarization-driven flux-closure polarization rotations in $PbTiO_3/SrTiO_3$ superlattices. We measure diffuse x-ray scattering in such superlattices down to 2.2 K and find diffuse signal fitting our simulations for flux-closure rotations, showing that these methods can be used to deduce the nature of periodic domain walls in ferroelectric layers. However, we do not find any experimental signatures of Bloch components down to 2.2 K for any of the layer thicknesses studied, and we discuss the implications of our measurements in the context of the recent studies performed on $PbTiO_3$ films.

Our theoretical and experimental work demonstrates that the presence of the Bloch component in the domain walls of $PbTiO_3$ is not guaranteed as previously thought and is instead extremely sensitive to the boundary conditions of the system. These results should serve as a starting point to inspire more investigations into the precise structure of ferroelectric domain walls in $PbTiO_3$ thin films and will further establish diffuse x-ray scattering studies as an indispensable tool for the characterization of complex polarization rotations.

II. FIRST- AND SECOND-PRINCIPLES STUDY OF FERROELECTRIC DOMAIN WALLS IN $PbTiO_3$ AND $PbTiO_3/SrTiO_3$ SUPERLATTICES WITHIN THE GENERALIZED GRADIENT APPROXIMATION

Previous first- and second-principles simulations of 180° domain walls in bulk $PbTiO_3$ and $PbTiO_3/SrTiO_3$ superlattices have found sizable Bloch components in their centers, with magnitudes reaching 0.6 C/m^2 [13,16,17] (These estimates in C/m^2 were calculated considering a one-unit-cell-thick domain wall centered on a PbO plane). Using second-principles simulations with a model constructed from first-principles data within the local density approximation (LDA), Wojdeł and Íñiguez found that the domain wall polarization persists beyond room temperature, with its own ferroelectric-to-paraelectric transition at approximately 340 K [13]. However, they highlighted the limits of using an LDA-based model to describe the domain wall transition, as this approximation overstabilizes the ferroelectric polarization in the domain walls [13]. To verify these predictions, we repeat similar first- and second-principles calculations using the GGA-PBEsol approximation, which provides a more accurate description of the physical properties of insulating perovskites compared to LDA [18,19].

We start with 180° domain walls in bulk $PbTiO_3$. For our density functional theory (DFT) calculations, we use a $12 \times 1 \times 1$ supercell [Fig. 1(a)] including domains of oppositely oriented polarization separated by domain walls centered on PbO planes, which appears to be the most stable configuration [20]. In this supercell, the domain polarization is in the z direction, and the domain wall Bloch polarization is in the y direction. Similarly to Ref. [13], we find that the domain wall energy is lower when we allow the domain wall to polarize (173.1 mJ/m^2 in the Bloch case versus 179.5 mJ/m^2 in the Ising case). The relaxed structure and the corresponding layer-resolved polarization profiles along y and z are shown in Figs. 1(b) and 1(c), respectively. Our DFT calculations are therefore consistent with previous studies and predict a sizable Bloch component in the 180° domain walls of unstrained, freestanding $PbTiO_3$ with a polarization $P_z = 0.93$ C/m^2 at the center of the domain, and a polarization $P_y = 0.40$ C/m^2 at the center of the domain wall at 0 K.

Because of the out-of-plane polarization along z, we observe a relative shift $\Delta z_{Pb} = 61$ pm of the Pb ions between up and down domains [20,21], as shown in Fig. 1(b). This shift is in agreement with the value calculated by Meyer and Vanderbilt [20] and comparable to the experimentally observed shift in thin films of $PbTiO_3$ [15]. Additionally, Fig. 1(b) shows that, as reported from previous first-principles studies [13,16], the domain wall polarization arises mostly from the displacement of the Pb atoms in the y direction. The shift of the Pb atoms is

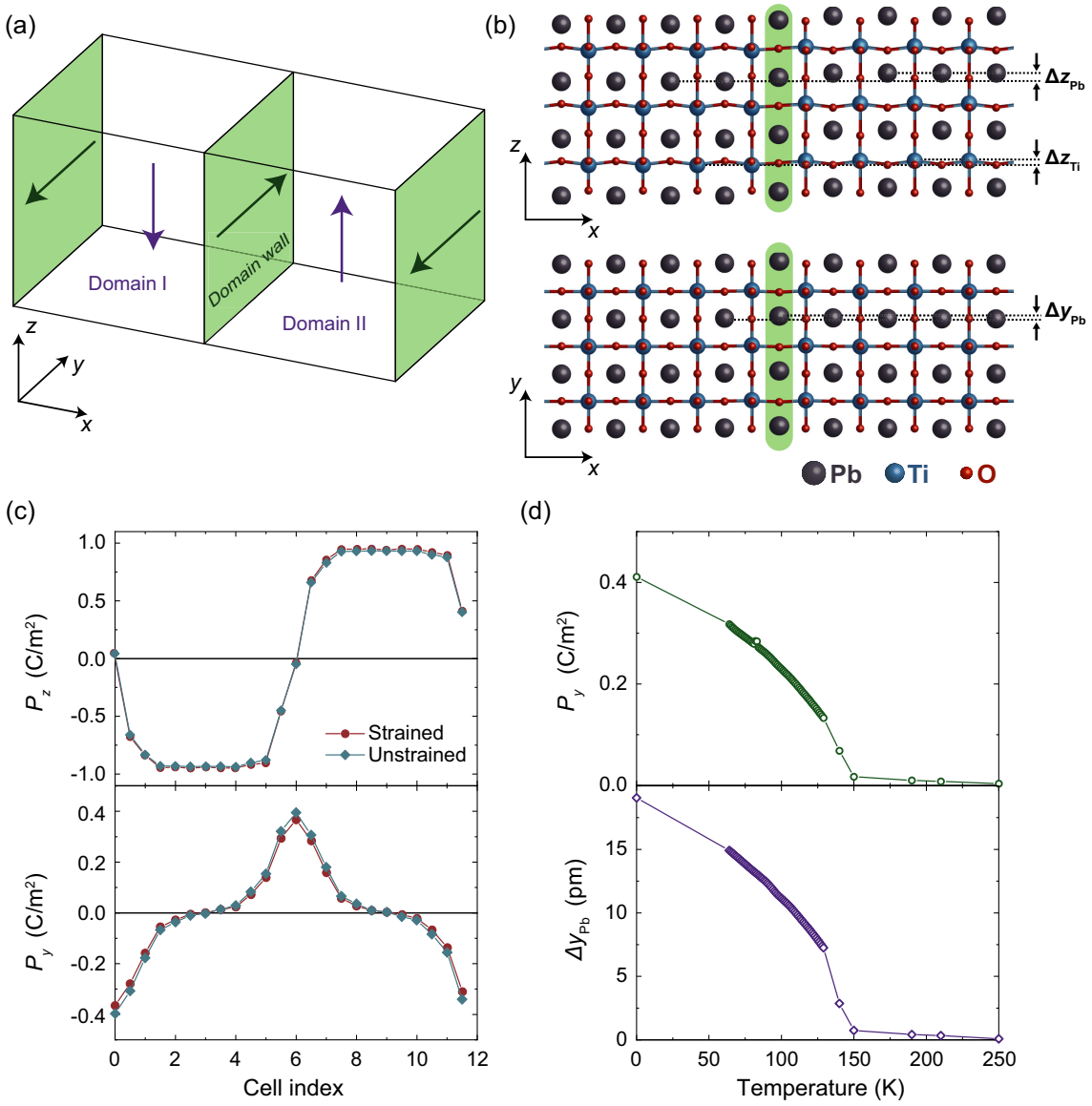

FIG. 1. First- and second-principles calculations of the structure of 180° domain walls in bulk $PbTiO_3$. (a) Sketch of the relative orientations of the polarization in the domains and domain walls of the supercells used in the first- and second-principles simulations. The polarization in the center of each domain points along the z direction, whereas a polarization in the plane of the wall (Bloch polarization) points along the y direction. (b) Lowest-energy structure for freestanding $PbTiO_3$, viewed in the x-z (top) and x-y (bottom) planes. The polarization inside the domains leads to a displacement of the Pb and Ti cations along z, equal to $\Delta z_{Pb} = 61$ pm and $\Delta z_{Ti} = 32$ pm between up and down domains, respectively. The polarization inside the domain wall leads to a Pb displacement along y, equal to $\Delta y_{Pb} = 20$ pm. The shaded green region marks the position of the 180° domain wall. (c) Layer-resolved polarization in the z (top) and y (bottom) directions for freestanding $PbTiO_3$ (blue diamonds) and for $PbTiO_3$ strained on $SrTiO_3$ (red circles). The plot shows that the polarization along the y direction reaches values of 0.4 C/m^2 inside the center of the domain walls and remains largely unchanged upon application of strain. (d) Second-principles calculations of the temperature dependence of the magnitude of the individual domain wall polarization, P_y (top), and the magnitude of the average Pb displacement in the domain wall, Δy_{Pb} (bottom), for $PbTiO_3$ strained on $SrTiO_3$, showing a ferroelectric-to-paraelectric transition occurring inside the domain wall at approximately 150 K. For the first-principles calculations, a $12 \times 1 \times 1$ supercell was used. For the second-principles calculations, a $20 \times 12 \times 12$ supercell was used.

approximately $\Delta y_{Pb} = 20$ pm [indicated in Fig. 1(b)], comparable to the observed Ti displacement in the tetragonal phase of $BaTiO_3$ [22,23] and in $PbTiO_3$ at room temperature [24].

The Pb displacement along y produces some pressure to elongate the unit cell along the b axis. Consistently, our relaxed supercell adopts the following lattice parameters at 0 K: $a = 3.892$ Å, $b = 3.897$ Å, $c = 4.075$ Å. This

implies that, when $PbTiO_3$ is strained on cubic $SrTiO_3$ (with lattice parameter of 3.889 Å as calculated using DFT), the Bloch component might be affected. To investigate this possibility, we simulate $PbTiO_3$ strained on $SrTiO_3$ by fixing the size of the a and b lattice constants to 3.889 Å. Interestingly, the predicted values of the polarization remain largely unchanged, with the polarization inside the domain increasing slightly to $P_z = 0.95$ C/m^2 and the Bloch polarization inside the domain wall decreasing only slightly to $P_y = 0.37$ C/m^2 [Fig. 1(c)], and with the corresponding Pb displacement in the domain wall decreasing to $\Delta y_{\mathrm{Pb}} = 19$ pm.

As stated above, we find from our DFT GGA-PBEsol calculations that the fully relaxed configuration at 0 K with Bloch polarization is lower in energy than without Bloch polarization by 6.4 mJ/m^2 = 6.5 meV/□ (for a $12 \times 1 \times 1$ supercell; meV/□ denotes energy per unit cell surface area of the domain wall). This energy difference is similar to that calculated by Wojdeł and Íñiguez using the same GGA-PBEsol functional (4 meV/□ using a $20 \times 1 \times 1$ supercell), but significantly smaller than that derived from their second-principles model built on the LDA (86 meV/□ using a $20 \times 1 \times 1$ supercell) [13]. As discussed in their work, the overestimate of the energy difference by their model indicates that the real ferroelectric-to-paraelectric transition temperature in the domain wall could be significantly smaller than the predicted temperature of 340 K [13]. In order to better estimate the temperature at which the Bloch polarization should disappear, we construct a new second-principles model relying on our GGA-PBEsol calculations (see Sec. VII).

To compare our new second-principles model with previous DFT calculations, we first employ the same $12 \times 1 \times 1$ supercell, obtaining consistent results: The appearance of the nonzero domain wall Bloch polarization lowers the energy by 9.3 meV/□ and gives rise to a structure where the polarization in the middle of the domain is $P_z = 0.84$ C/m^2, the Bloch polarization in the domain wall is $P_y = 0.42$ C/m^2, and the Pb displacement in the domain wall is $\Delta y_{\mathrm{Pb}} = 19.5$ pm. To properly estimate the temperature evolution of the Bloch component of the polarization, we utilize a larger $20 \times 12 \times 12$ supercell (strained on $SrTiO_3$). Figure 1(d) shows the calculated domain wall Bloch polarization P_y and the corresponding magnitude of Δy_{Pb} as a function of temperature for bulk $PbTiO_3$. We find that P_y becomes zero at approximately 150 K, which, as expected, is below the temperature predicted in Refs. [8,13] but remains quite high. Interestingly, we note that for freestanding $PbTiO_3$ (no imposed strain), we find a transition temperature equal to approximately 200 K.

We now move from pure $PbTiO_3$ to (001)-oriented $PbTiO_3/SrTiO_3$ superlattices [from now on we will denote these systems with $(\mathrm{PTO_n}|\mathrm{STO_m})_\mathrm{N}$, where n and m are the number of unit cells of $PbTiO_3$ and $SrTiO_3$ per period, respectively, and N is the number of repetitions]. The $PbTiO_3$ layer is now sandwiched between $SrTiO_3$ layers, limiting the extension of the domain wall in the z direction. In this case, the incomplete screening of the depolarizing field by the $SrTiO_3$ layer typically gives rise to flux-closure domains [21]. Using the second-principles model of Wojdeł and Íñiguez constructed on LDA data, Ortiz and coworkers explored the evolution of the polar textures with layer thicknesses, epitaxial strain, and temperature [17,25]. They predicted the presence of a Bloch component of polarization in domain walls up to room temperature, which further appeared as a key feature to explain the formation of polar skyrmions [8]. However, other simulations of $PbTiO_3$ thin films using LDA [26], and alternative models for domain walls in $(\mathrm{PTO_{10}}|\mathrm{STO_{10}})_\infty$ relying on the GGA-PBEsol functional [27], did not report any Bloch component. To gain more insight, we take our $PbTiO_3$ and $SrTiO_3$ second-principles bulk models built on GGA-PBEsol data and combine them according to previously proposed methodology [28] to reinvestigate $PbTiO_3/SrTiO_3$ superlattices.

As a prototypical example, we consider $(\mathrm{PTO_6}|\mathrm{STO_6})_\infty$ superlattices epitaxially grown on a $SrTiO_3$ cubic substrate. For such layer thicknesses, our calculations find that the equilibrium domain period (Λ_d) is approximately 18 unit cells (see Supplemental Material Fig. 1 [29]; for comparison, other calculations found an equilibrium domain period of 12–14 unit cells at these thicknesses [25]). Importantly, as shown in Fig. 2, while we observe the presence of a Bloch component in the domain wall for small lateral domain sizes ($P_y = 0.27$ C/m^2 for $\Lambda_d = 8$ unit cells), this component progressively reduces with increasing Λ_d and disappears completely for domain periods larger than 14 unit cells. Consistently, we find that the Bloch component disappears completely at periods lower than the equilibrium domain periods of superlattices with different layer thicknesses. Figure 2(c) shows a plot of the magnitude of the Bloch component as a function of domain period for bulk $PbTiO_3$ and for superlattices with varying thickness of $PbTiO_3$ and $SrTiO_3$, specifically $(\mathrm{PTO_6}|\mathrm{STO_6})_\infty$, $(\mathrm{PTO_{10}}|\mathrm{STO_6})_\infty$, and $(\mathrm{PTO_{10}}|\mathrm{STO_{10}})_\infty$. At the equilibrium domain period for each system (18, 26, and 24 unit cells, respectively, marked by the vertical arrows) the magnitude of the Bloch component is zero.

The absence of Bloch polarization at the domain walls of the superlattices is consistent with simulations on $PbTiO_3/SrTiO_3$ using machine learning potentials [27]. However, it is at odds with our predictions for bulk $PbTiO_3$, for which the Bloch component is largely independent of the lateral size of the domains. The disappearance of the Bloch component in our superlattices is most likely related to the finite size of the $PbTiO_3$ layer in the simulated $PbTiO_3/SrTiO_3$ superlattices (in contrast to bulk $PbTiO_3$) and appears to originate from the interaction between the Bloch and flux-closure components of the polarization.

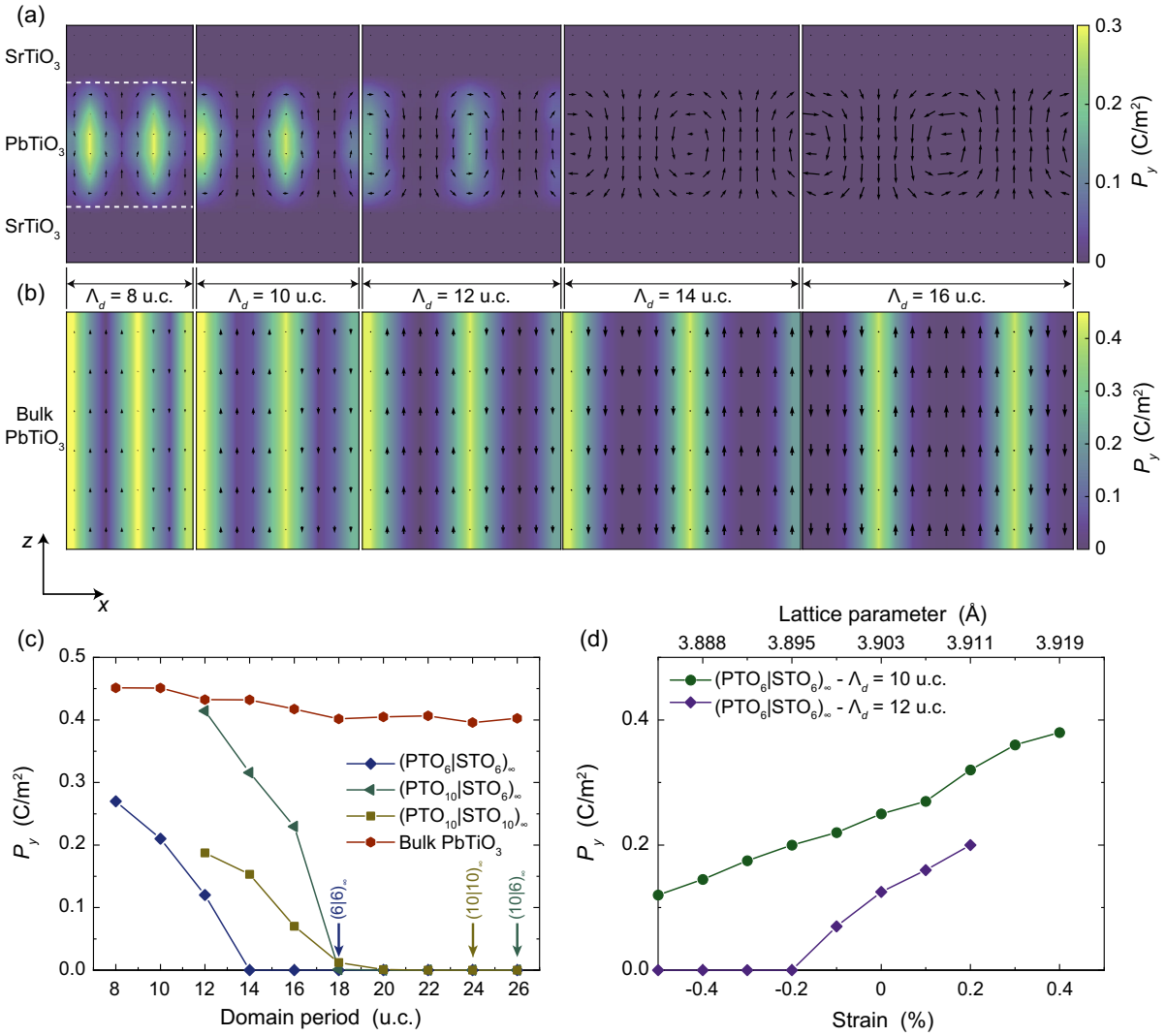

FIG. 2. Second-principles calculations of the structure of 180° domain walls in $PbTiO_3/SrTiO_3$ superlattices at 0 K. (a) Cross sections of a $(PTO_6|STO_6)_\infty$ superlattice period viewed in the x-z plane for domain periods ranging from 8 to 16 unit cells. The color scales depict the magnitude of P_y, whereas the arrows mark the orientation of the spontaneous polarization. The Bloch polarization in the centers of the 180° domain walls decreases in magnitude with increasing domain period and disappears between 12 and 14 unit cells. (b) Domain period dependence of the Bloch polarization in bulk $PbTiO_3$ for comparison. No significant changes in the Bloch component occur. Note the different color scale compared to (a). (c) Plot of the magnitude of the Bloch polarization in the domain walls of bulk $PbTiO_3$ (red circles) and for $PbTiO_3/SrTiO_3$ superlattices with different layer thicknesses as a function of the domain period (both systems are strained on $SrTiO_3$). The arrows indicate the equilibrium domain periods for the $PbTiO_3$ layer in each superlattice. The Bloch polarization is systematically zero at the equilibrium domain period. (d) Plot of the Bloch polarization in the domain walls of the $PbTiO_3/SrTiO_3$ superlattice as a function of strain, for a domain period of 10 (green circles) and 12 (purple diamonds) unit cells.

Consecutive panels in Fig. 2(a) demonstrate that, as the domain period Λ_d progressively increases, the volume occupied by the flux closure regions naturally expands to eventually cover the entire film thickness and suppress the Bloch component. In the bulk $PbTiO_3$ calculations with periodic boundary conditions [Fig. 2(b)], which artificially remove the surface region, the Bloch component remains sizable ($P_y = 0.38$ C/m^2 at $\Lambda_d = 130$ unit cells), confirming the intrinsic Bloch nature of the domain wall in $PbTiO_3$ and supporting our interpretation of a surface effect in $PbTiO_3/SrTiO_3$ superlattices.

Importantly, we also observe that the magnitude of the Bloch component is strongly sensitive to the epitaxial strain as shown in Fig. 2(d). For a domain period of 12 unit cells, the Bloch component disappears when we increase the compressive strain from 0 to −0.2% (see Sec. VII for the definition of the lattice parameters for the $PbTiO_3/SrTiO_3$ system). From a modeling perspective, these observations mean that making reliable predictions remains challenging since the results might be very sensitive to the approximations that are used and the way the strain is treated in the simulations. Experimentally, it means that partial relaxation

of the superlattice and local fluctuation of the strain (e.g., during preparation of lamellae for STEM analysis) might strongly affect the observations. Nevertheless, we note that the use of tensile strain to attempt to stabilize the Bloch component in $PbTiO_3$ domain walls is associated with caveats that must be considered. Substrates that impose tensile strain on $PbTiO_3$ (including the rare-earth scandates) also promote the formation of *a*–*c* domains due to ferroelasticity [30]. The combination of the depolarizing field and the tensile strain induces asymmetric flux-closure arrays with net in-plane polarization, where 90° and 180° domain walls coexist [27,31]. The ferroelastic component in the tensile strain regime could further affect the Bloch component in the 180° domain walls. However, as our work considers only the structure of 180° domain walls, we will consider the compressive strain regime and focus on multilayers deposited on $SrTiO_3$ substrates.

In summary, our calculations based on the GGA-PBEsol functional are consistent with previous studies and confirm the presence of a Bloch component in bulk $PbTiO_3$ 180° domain walls. This method allowed us to obtain a more reliable estimate of the temperature at which the Bloch component should disappear. Furthermore, our theoretical analysis supports the possibility of a Bloch component developing in the 180° domain walls of $PbTiO_3/SrTiO_3$ superlattices. We find a strong and previously unreported sensitivity of this component to the ferroelectric domain periodicity and the epitaxial strain. These findings suggest that the presence of a Bloch component in $PbTiO_3/SrTiO_3$ superlattices might not be ubiquitous and, if present, may be more challenging to detect than previously thought.

III. PHASE-FIELD SIMULATIONS OF LABYRINTHINE 180° DOMAIN WALLS IN $PbTiO_3/SrTiO_3$ SUPERLATTICES

To explore more realistic domain structures with labyrinthine domain wall orientations, a larger volume of the material must be calculated. One of the most convenient models by which polarization distributions over several millions of unit cells can be simulated is the Ginzburg-Landau-Devonshire model with long-range electrostatic interactions, a method known as phase-field simulations. The phase-field model is a greatly simplified description of the materials in question, and there are no standard protocols to determine phase-field model parameters. For this reason, we do not use the phase-field model for a direct prediction of such subtle phenomena like the Bloch-to-Ising domain wall transition in superlattices. On the other hand, phase-field simulations can be conveniently used to predict specific features of diffuse x-ray scattering patterns related to the presence or absence of Bloch components within realistic domain structure configurations (and so determine whether the Bloch component exists or not by comparison with real diffraction experiments, as will be seen later).

Our phase-field simulations were performed using the program FERRODO (see Sec. VII). The system chosen is a $(PTO_{13}|STO_5)_{12}$ superlattice under a compressive epitaxial strain of -1.5% with respect to the cubic paraelectric phase of $PbTiO_3$, thus simulating the constraint imposed by a $SrTiO_3$ substrate. Figure 3(a) shows the calculated three-dimensional structure, which exhibits a labyrinthine domain pattern with 180° domain walls and a domain period equal to approximately 27 unit cells. This type of labyrinthine structure is consistent with experimentally observed domain wall patterns in $PbTiO_3$ thin films and multilayers deposited on low-miscut $SrTiO_3$ substrates [8,32–36], as well as other reports of systems with modulated phases [37]. The domain walls in the simulated $PbTiO_3/SrTiO_3$ system are mostly aligned along the whole thickness of the superlattice, signifying a large degree of coherence in the out-of-plane direction, most likely as a result of structural and/or electrostatic coupling through the $SrTiO_3$ layers [38].

A cross section in the *x*-*z* plane of a single simulated $PbTiO_3$ layer is shown in Fig. 3(b), showing a flux-closure pattern. This pattern is characterized by a polarization that is directed out of plane at the centres of the domains and continuously rotates to in plane at the domain walls as well as near the top and bottom interfaces with $SrTiO_3$. The maximum magnitude of the polarization in the out-of-plane and in-plane direction is 0.7 C/m^2 and 0.45 C/m^2, respectively. These values imply that while the term "flux closure" is used for simplicity, the flux does not close completely, and an excess out-of-plane polarization remains in the center of each domain at the interfaces between $PbTiO_3$ and $SrTiO_3$. The domains are symmetric such that the $-P_x$ and $+P_x$ regions occupy the same volume and have the same magnitudes of polarization, in contrast to tensile-strained $PbTiO_3$ thin films and multilayers on $GdScO_3$ [6] and $DyScO_3$ [7].

The *x*-*y* cross sections of the same simulated $PbTiO_3$ layer at *z* positions corresponding to the middle of the layer and the top interface with $SrTiO_3$ are plotted in the left-hand and right-hand panels of Fig. 3(c), respectively. No in-plane polarization components are visible in the middle of the $PbTiO_3$ layer, while at the top interface the in-plane polarization is perpendicular to the domain walls, consistent with the flux-closure configuration inferred from Fig. 3(b). Therefore, no Bloch components emerge from our phase-field simulations, in agreement with our second-principles calculations on $PbTiO_3/SrTiO_3$ superlattices with their equilibrium domain periods.

For the following discussion it is useful to consider an artificially designed domain structure identical to the above simulated domain structure, but with Ising domain walls replaced by Bloch domain walls. We have constructed this artificial structure by using the as-received polarization pattern and superposing onto it an additional in-plane polarization field, calculated from the gradient of the

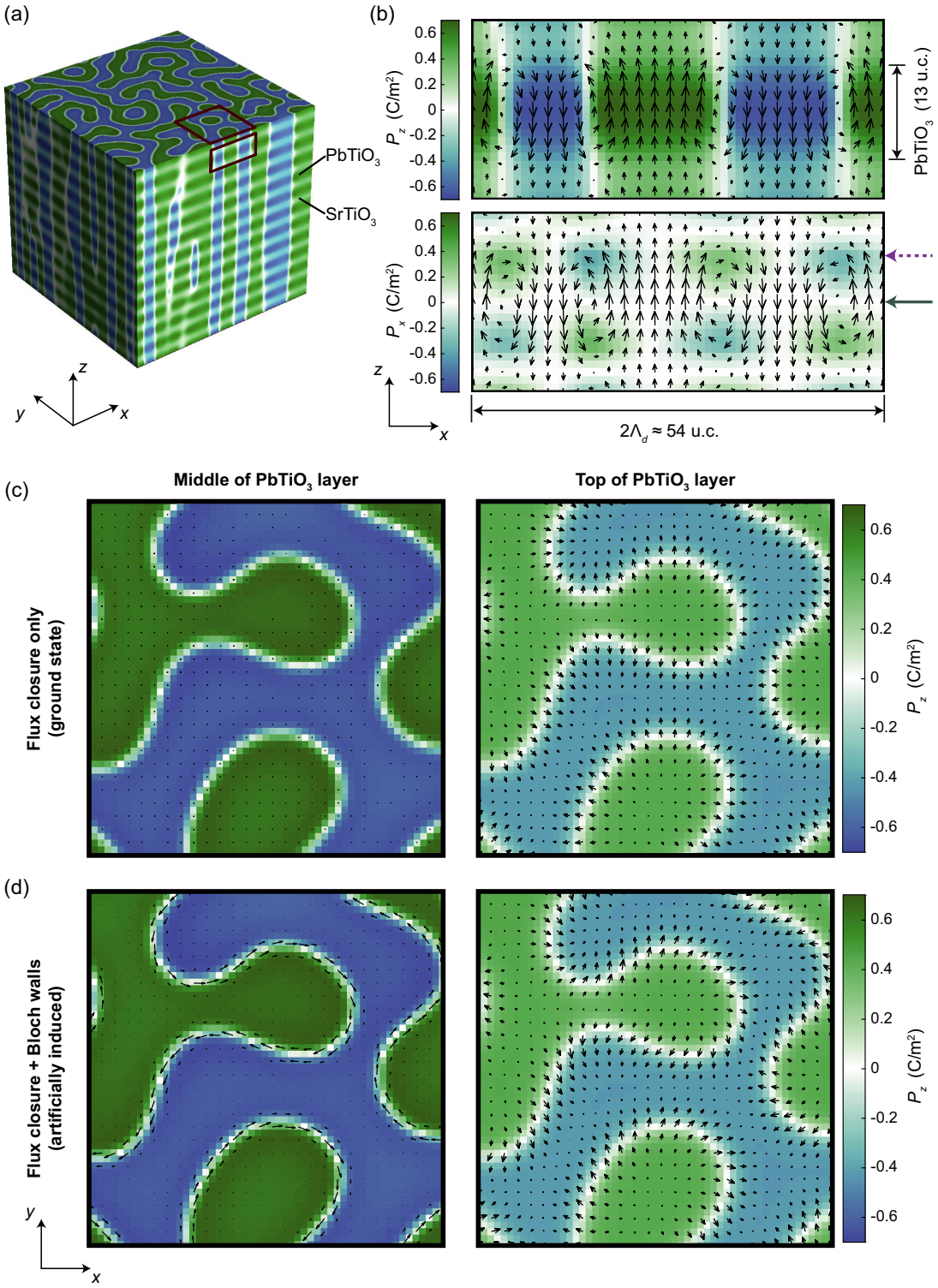

FIG. 3. Phase-field simulations of the domain structure in a $(PTO_{13}|STO_5)_{12}$ superlattice. (a) Simulated 3D distribution of the polarization component in the z direction P_z for a superlattice with 12 periods of 13 unit cells of $PbTiO_3$ and 5 unit cells of $SrTiO_3$, with the middle of the $PbTiO_3$ layer at the top of the supercell. (b) Cross section of a superlattice period viewed in the x-z plane in the region marked by the rectangle in (a). The color scales depict the magnitude of P_z (top) and P_x (bottom), whereas the arrows mark the orientation of the spontaneous polarization. The bottom panels correspond to the polarization distribution in the x-y plane for (c) the ground state structure with only a flux-closure-type polarization rotation, and (d) a structure with artificially induced Bloch components in the centers of the domain walls. The left- and right-hand sides of each panel are cuts through the middle and top of the $PbTiO_3$ layer, marked by the solid and dashed arrows in (b), respectively. The color scales correspond to the magnitude of P_z, and the arrows to the direction of the polarization.

as-received out-of-plane polarization according to the expressions $P'_x = P_x - (\partial P_z/\partial y)|dy|$ and $P'_y = P_y + (\partial P_z/\partial x)|dx|$. The artificial Bloch polarization obtained is approximately equal to 0.55 C/m^2, comparable to our first-principles predictions for a domain wall in bulk $PbTiO_3$. The spatial distribution of polarization within this homochiral Bloch structure is plotted in Fig. 3(d). Here, the Bloch polarization parallel to the periodic domain walls is clearly visible in the cut through the middle of the $PbTiO_3$ layer (left-hand panel).

IV. CALCULATION OF DIFFUSE SCATTERING FROM PHASE-FIELD POLARIZATION PATTERNS

Phase-field simulation data can be used to model the characteristic diffuse scattering fingerprints from different polarization patterns. The scattered x-ray amplitude $F(\boldsymbol{Q})$ from a ferroelectric crystal with 180° domain walls can be computed as

$$F(\boldsymbol{Q}) = \sum_{j}^{\text{crystal}} f_j \exp[-i\boldsymbol{Q}\cdot(\boldsymbol{r}_{0j} + \delta\boldsymbol{r}_j)], \qquad (1)$$

where the sum is over all atoms in the crystal structure, $\boldsymbol{Q}$ is the scattering vector, f_j is the form factor of atom j in the parent centrosymmetric structure, and $\delta\boldsymbol{r}_j$ the displacement of the atom from its equilibrium position $\boldsymbol{r}_{0j}$ with respect to the centrosymmetric state due to the local polar distortions $\boldsymbol{p_a}$ and local acoustic displacements $\boldsymbol{u}$ (see Sec. VII).

This equation entails that the scattered intensity will be modulated due to the presence of 180° domain walls when the scalar product between the scattering vector $\boldsymbol{Q}$ and the atomic displacement $\delta\boldsymbol{r}_j$ is nonzero [32,33]. Therefore, for an ideal labyrinthine 180° domain pattern with no in-plane polarization components we expect no diffuse signal around $HK0$ pseudocubic Bragg peaks for which $Q_z = 0$, and an isotropic ring of diffuse intensity around HKL reflections with $L \neq 0$, for which $Q_z \neq 0$ [36]. Conversely, when in-plane components are present and $\delta\boldsymbol{r}_j$ has nonzero x and y components, diffuse signal will also be observed around $HK0$ reflections and will necessarily be anisotropic because of the scalar product in Eq. (1). The exact shape of this anisotropy will depend on whether the polarization components are perpendicular or parallel to the domain walls (see Supplemental Material Fig. 2 [29]) and therefore encodes information on the precise nature of the polarization texture being probed.

We thus proceed to calculate the diffracted intensity $|F(\boldsymbol{Q})|^2$ from our simulated Ising-like and artificially induced Bloch wall domain patterns by substituting the corresponding atomic positions into Eq. (1) (see Sec. VII). The resulting intensity distribution in the $0KL$ reciprocal space plane arising from the Ising-like structure is shown in Fig. 4(a). Along the out-of-plane direction, the repeating unit of this superlattice consists of 18 unit cells, giving rise to 18 superlattice Bragg peaks up to $L = 1$. For clarity throughout the paper, we index superlattice reflections with lowercase indices hkl, whereas for the $SrTiO_3$ substrate peaks in the subsequent experimental sections we use HKL. As expected, superlattice Bragg peaks with $Q_z \neq 0$ are accompanied by diffuse signal due to the periodicity of the 180° domain walls in our simulated labyrinthine structure in Fig. 3(a). The distance between the diffuse and the superlattice peaks is $\Delta H = 0.037$ r.l.u., corresponding to a simulated domain period $\Lambda_d = (1/\Delta H) = 27$ u.c. (where u.c. denotes the unit cell of the phase-field derived structure with the reference lattice constant 0.4 nm; see Sec. VII).

Figures 4(b) and 4(c) show the $hk0$ (top) and $hk1$ (bottom) planes obtained from simulated patterns with the Ising-like flux closure and artificially induced Bloch wall textures, respectively. The $hk1$ planes of both textures are qualitatively similar and are consistent with the scenario sketched in Supplemental Material Fig. 2(b) [29], which depicts the diffuse signatures of a domain pattern with polarizations perpendicular to the plane of the domain walls. This diffuse signal comes from in-plane components of the flux-closure pattern near the $PbTiO_3/SrTiO_3$ interfaces (see Fig. 3). On the other hand, inspection of the $hk0$ planes reveals that the flux-closure pattern gives rise to weak second order diffuse intensity with maxima along the scattering vector $\boldsymbol{Q}$, whereas the pattern including Bloch polarization gives rise to additional strong transverse diffuse signal. This strong transverse diffuse signal is consistent with a domain pattern with polarizations parallel to the plane of the domain walls (i.e., Bloch walls) as depicted in Supplemental Material Fig. 2(a) [29].

Figures 4(d) and 4(e) are detailed plots of the calculated diffuse signal in the HK plane around the 100 ($L = 0$), 101 ($L = 0.06$ r.l.u.), and 1054 ($L = 3$) superlattice peaks for the cases of flux-closure domain walls with no polarization in the center of the domain wall and for flux-closure walls with Bloch polarization in the center of the domain wall, respectively. The middle and bottom rows are calculations in which contributions from local polar distortions $\boldsymbol{p_a}$ (indicated as polarization only) and local acoustic displacements $\boldsymbol{u}$ (indicated as strain only) have been isolated.

The separated contributions give similar diffuse features. The maps derived from local acoustic displacements ("strain only") show broadening of Bragg and superlattice reflections (which will be discussed further below), and weak second order diffuse intensity. The second order diffuse scattering, corresponding to a period equal to $(\Lambda_d/2) = 13$ u.c., arises from the electrostriction related strain contrast, which gives the mean size of simulated domains. However, when we consider only the effect of polar distortions ("polarization only"), we see that the diffuse signal around the 100 superlattice peak disappears, as the contributions to the structure factor from the top and

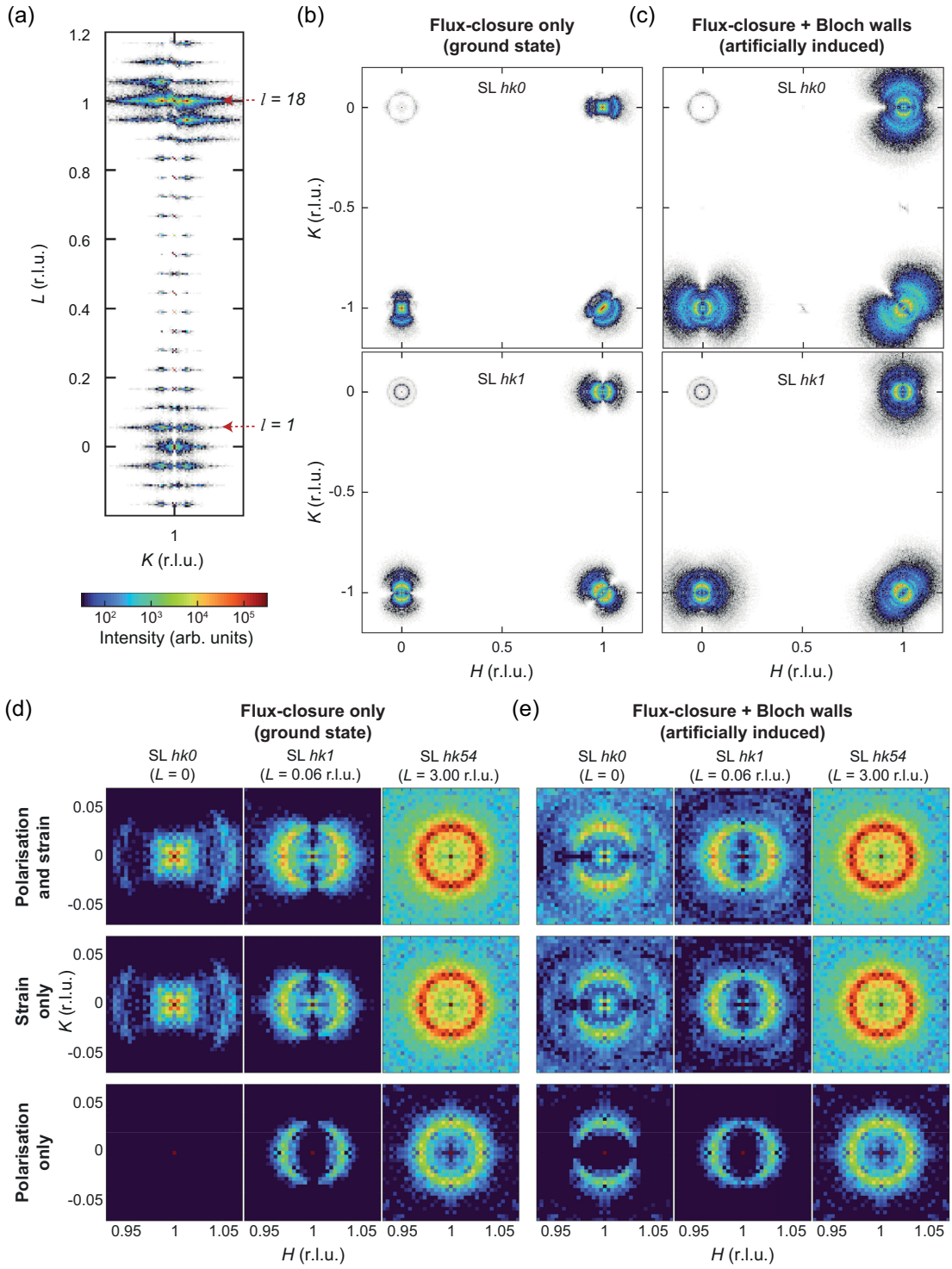

FIG. 4. Diffuse scattering calculations for nanoscale flux-closure domain walls for the Ising and artificially induced Bloch case, and the comparison of lattice distortion versus polarization. Calculated diffuse scattering intensity map in the $0KL$ plane of the $(PTO_{13}|STO_5)_{12}$ superlattice simulated in Fig. 3. $l = 1, \ldots, 18$ superlattice peaks occur between $L = 0$ and $L = 1$. Diffuse scattering appears around each superlattice Bragg peak due to the periodic domain structure. Diffracted intensity in the HK plane around the $hk0$ (top) and $hk1$ (bottom) superlattice peaks for the case of (b) Ising and (c) artificially induced Bloch domain walls. The Bloch component gives rise to an anisotropic diffuse scattering pattern around the $hk0$ peaks, with minima parallel to the in-plane component of the scattering vector Q_{IP}. The flux-closure domain configuration gives rise to anisotropic diffuse scattering around the $hk1$ superlattice peaks with minima perpendicular to Q_{IP}. (d),(e) Short-range simulated diffraction patterns for the Ising and Bloch cases respectively, when both acoustic distortions and polar distortions are considered (top row), when only the effect of the acoustic distortion is isolated (middle row), and when only polar distortions are isolated (bottom row).

bottom part of the $PbTiO_3$ layer cancel [see variation of the P_x component in Fig. 3(b)].

Our calculations demonstrate that by measuring diffuse signal around Bragg peaks with $L = 0$ we can distinguish between an Ising configuration or a configuration with Bloch polarization in the 180° domain walls of $PbTiO_3$ layers in $PbTiO_3/SrTiO_3$ superlattices. We note that similar guidelines were successfully applied to detect Bloch (and Néel) domain walls in magnetic single crystals and multilayers using resonant soft x-ray diffraction (RSXD) [39–43]. Furthermore, we also show that diffuse signal around peaks with nonzero but small values of l is sensitive to the nanoscale polarization rotation driven by the depolarizing field in the 180° domain walls of ultrathin $PbTiO_3$. Careful study of the diffuse scattering around these peaks will therefore allow for such nanoscale polarization rotation to be probed via x-ray scattering techniques.

V. DIFFUSE X-RAY SCATTERING STUDIES OF THE STRUCTURE OF FERROELECTRIC DOMAIN WALLS IN $PbTiO_3$

To determine the polarization configuration of the ferroelectric domain walls in $PbTiO_3/SrTiO_3$ superlattices deposited on $SrTiO_3$ substrates, we perform measurements at the ID28 diffuse x-ray scattering end station at ESRF (see Sec. VII) and compare the results to the schematic outlines above. The $0KL$ reciprocal space plane of a $(PTO_{16}|STO_5)_{11}$ superlattice at room temperature is shown in Fig. 5(a). The coordinates are expressed in reciprocal lattice units of $SrTiO_3$, where $= 3.905$ Å [to convert from r.l.u. to $Å^{-1}$, the values should be multiplied by $(2\pi/3.905)$ $Å^{-1}$]. Note that unlike fine period superlattices, only peaks at integer values of K are present, indicating that there is no doubling of the pseudocubic unit cell along the in-plane directions due to antiferrodistortive structural ordering and/or improper ferroelectricity [44,45].

Figures 5(b) and 5(c) show the superlattice peaks around $K = -1$ and $K = 1$ in more detail. The repeating superlattice unit consists of 21 perovskite unit cells with an average out-of-plane lattice parameter $c_{SL} = (c_{STO}n_{STO} + c_{PTO}n_{PTO})/(n_{STO} + n_{PTO})$, where c_{STO}, c_{PTO} are the out-of-plane lattice parameters of the $SrTiO_3$ and $PbTiO_3$ layers, respectively, and n_{STO}, n_{PTO} are the numbers of unit cells of $SrTiO_3$ and $PbTiO_3$ per repetition. Because of the similar values of c_{STO} and c_{PTO}, there are 21 superlattice Bragg peaks up to $L = 1$, and these peaks are indexed accordingly. The first superlattice Bragg peak ($l = 1$) then occurs at $L = 0.046$ r.l.u., and the 21st superlattice Bragg peak ($l = 21$) at $L = 0.970$ r.l.u. The diffuse signal arising from periodic 180° domains occurs at $\Delta K = 0.035$ r.l.u., and corresponds to a domain period $\Lambda_d = 110$ Å.

Figure 5(d) shows a subsection of the $hk0$ plane for the $(PTO_{16}|STO_5)_{11}$ superlattice ($l = 0$, $L = 0$). No diffuse signal is observed around the 100, $0\bar{1}0$, and $1\bar{1}0$ peaks of the superlattice, in line with other x-ray diffraction experiments on ferroelectric domains in $PbTiO_3$ thin films deposited on $SrTiO_3$ [32]. Conversely, around the $hk1$ superlattice peaks ($l = 1$, $L = 0.046$ r.l.u.), shown in Fig. 5(e), we observe clear diffuse intensity arising from the periodic domain structure, with minima in intensity along a direction perpendicular to the in-plane component of the scattering vector Q_{IP}. Given that the second order signal around the $hk0$ peaks in Fig. 4(d) is predicted to be very weak, and is likely not detectable experimentally in our setup, we find that the experimentally observed diffuse patterns are entirely consistent with the nanoscale flux-closure structure found as the ground state of our phase-field simulations.

Additional higher resolution measurements performed at beamline ID01, ESRF on a $(PTO_{13}|STO_5)_{12}$ superlattice with domain period $\Lambda_d = 90$ Å (Fig. 6) confirm the absence of diffuse scattering around the $l = 0$ reflections and identical anisotropic diffuse scattering around the $l = 1$ peaks. The signals additionally appear to be independent of the $SrTiO_3$ layer thickness, as high-resolution room-temperature measurements for a $(PTO_{13}|STO_{12})_{10}$ ($\Lambda_d = 80$ Å) and a $(PTO_{16}|STO_{12})_9$ ($\Lambda_d = 100$ Å) superlattice exhibit identical features (or absence thereof) around the $l = 0$ and $l = 1$ reflections (Supplemental Material Fig. 3 [29]).

Furthermore, with the improved resolution we can observe additional structured diffuse signal close to the Bragg peaks with characteristic butterfly or rod shapes. This signal is consistent with Huang-like scattering [46] observed in a variety of systems: from materials with point defects and defect clusters [47] to systems exhibiting Jahn-Teller distortions [48]. Such scattering is not produced directly from local displacements, but from the long-range strain field that arises in the crystal lattice in response. Diffuse signal (broadening) with similar characteristic shapes is well captured by the acoustic displacement "strain" term of our calculations (Fig. 4) and most likely arises from the long-range response of the crystal lattice to the Pb and Ti displacements. However, the precise origin and details of this diffuse signal are beyond the scope of this work and, therefore, other than to note the general good agreement between theory and experiment, no further discussion is provided.

With increasing l, the diffuse scattering from the periodic domain structure becomes more isotropic. Figure 5(f) shows the $hk21$ plane ($l = 21$, $L = 0.970$ r.l.u.), where a diffuse ring is present, similar to previous reports on $PbTiO_3$ thin films [32,33] and $PbTiO_3/SrTiO_3$ superlattices deposited on $SrTiO_3$ substrates [8,36,49]. However, the intensity is not entirely isotropic, with enhanced intensity along the $\langle 100 \rangle$ directions, indicating a preference for $\{100\}$-oriented domain walls. Additionally, the fourfold symmetry of the diffuse signal is further reduced as the diffuse signals with positive and negative ΔK have different intensities, shown clearly in Supplemental Material

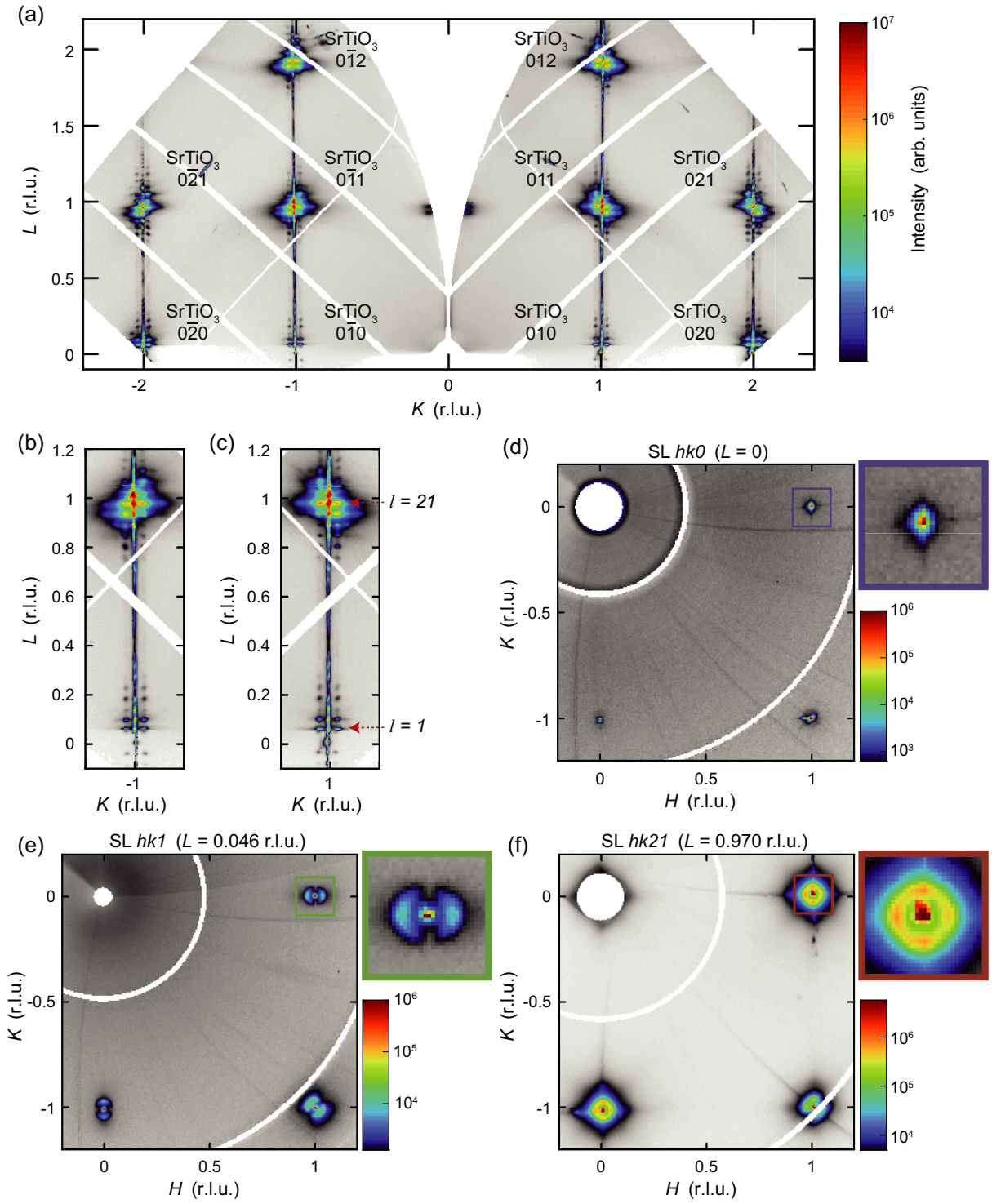

FIG. 5. Diffuse scattering measurements performed at beamline ID28, ESRF. (a) Reciprocal space map in the $0KL$ plane of a $(PTO_{16}|STO_5)_{11}$ superlattice deposited on $SrTiO_3$. Shorter-range maps around (b) $K = -1$ and (c) $K = 1$ show the $l = 1, \ldots, 21$ superlattice peaks between $L = 0$ and $L = 1$. Diffuse signal appears around each superlattice Bragg peak, exhibiting a left-right asymmetry. The color scale is identical to (a). (d) The HK plane around the $hk0$ superlattice peaks, where no diffuse signal is observed. (e) Diffuse signal around the $hk1$ superlattice peaks, showing an anisotropic diffuse scattering pattern with minima along a direction perpendicular to Q_{IP}. (f) Diffuse signal around the $hk21$ superlattice peaks, showing a nearly isotropic diffuse scattering ring. The boxes in (d)–(f) show high magnification views of the diffracted intensity around the 100, 101, and 1 0 21 superlattice peaks. Note that the $1\bar{1}21$ peak is partially obscured by the detector gap. The reciprocal space maps are plotted using a hybrid color scale to emphasize diffuse signal between Bragg peaks; the color bar next to each panel is logarithmic and the intensity below the minimum value of each color bar is expressed in linear gray scale. SL, superlattice; arb. units, arbitrary units.

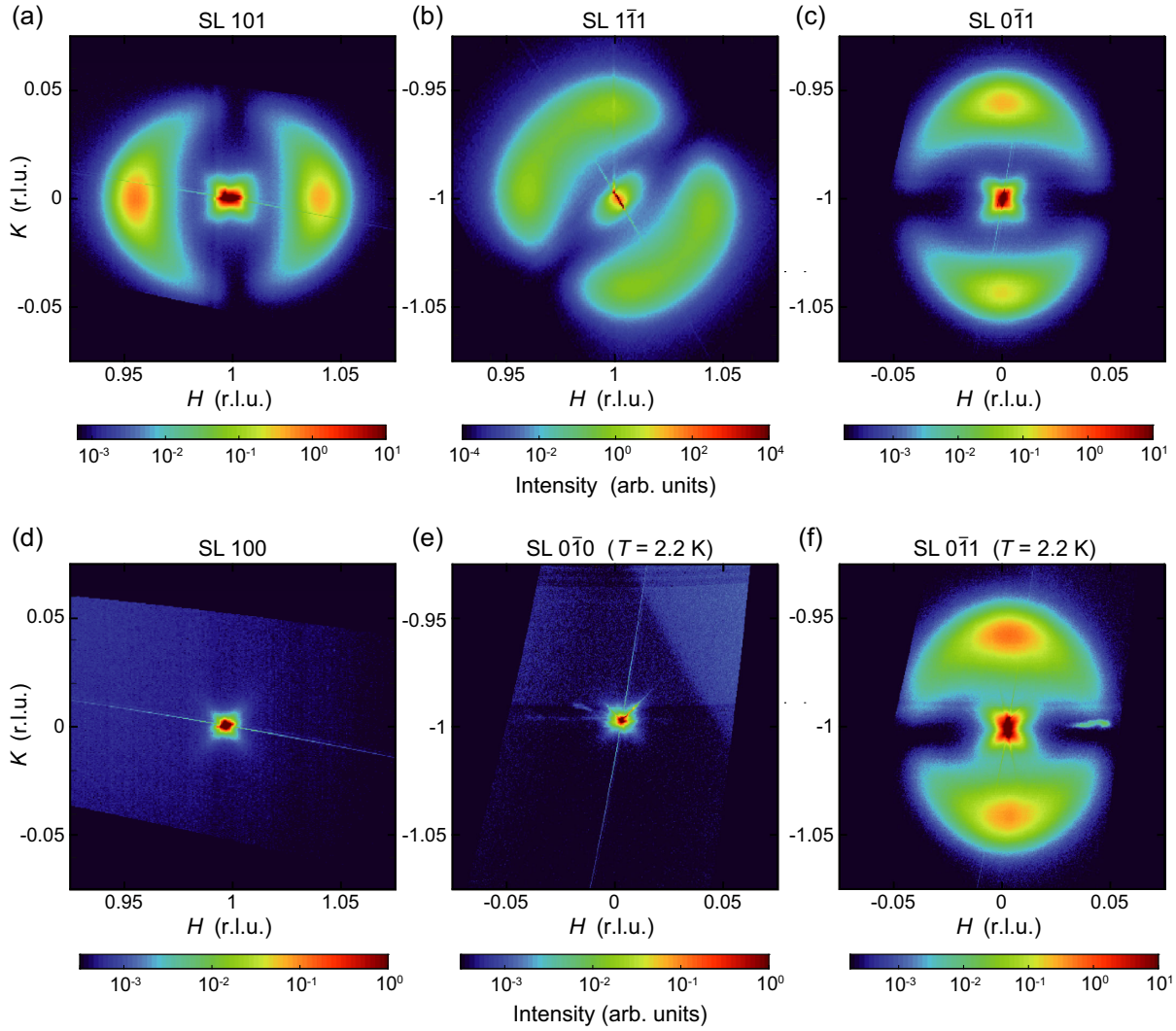

FIG. 6. High-resolution measurements at beamline ID01, ESRF for a $(PTO_{13}|STO_5)_{12}$ superlattice. Reciprocal space maps in the HK plane around the (a) 101 ($l = 1$, $L = 0.054$ r.l.u.), (b) $1\bar{1}1$, (c) $0\bar{1}1$, and (d) 100 ($l = 0$, $L = 0$) Bragg peaks of the superlattice, taken at room temperature. The minima in the diffuse scattering in (a)–(c) lie along a direction perpendicular to the in-plane component of the scattering vector Q_{IP}. No diffuse scattering is observed around the 100 peak. (e) Reciprocal space map around the $0\bar{1}0$ peak at 2.2 K. No diffuse scattering is observed around this peak at low temperatures. (f) Reciprocal space map around the $0\bar{1}1$ peak at 2.2 K, showing no qualitative change in the diffuse scattering at low temperatures (quantitative changes in the diffuse scattering are summarized in the Supplemental Material [29]).

Fig. 4 [29]. The anisotropy becomes less prominent with increasing L as demonstrated in Supplemental Material Fig. 5, where the $l = 54$ and $l = 1$ peaks are compared. Further diffuse scattering calculations (not shown here) demonstrate that this asymmetry is consistent with the combination of periodic out-of-plane and in-plane atomic displacements due to the in-plane polarization rotation at the 180° domain walls of the $PbTiO_3$ layers. Note that the apparent anisotropy around the $1\bar{1}21$ peak is an artifact arising from integration over the detector gap. Almost fully isotropic diffuse signal around this reflection was confirmed by measurements at a different detector position.

High-temperature measurements of the $0\bar{1}1$ and 0036 ($l = 36$, $L = 1.944$ r.l.u.) superlattice peaks for the $(PTO_{13}|STO_5)_{12}$ system (Supplemental Material Fig. 6 [29]) show that the diffuse signal around both peaks disappears at 723 K, due to the disappearance of the ferroelectric polarization and the 180° domain structure. Reducing the temperature to 2.2 K does not lead to any striking changes in the diffuse signal around the $0\bar{1}1$ superlattice peak for this $(PTO_{13}|STO_5)_{12}$ sample, nor the appearance of diffuse signal around the $0\bar{1}0$ superlattice peak [Figs. 6(e) and 6(f) and Supplemental Material Fig. 7 [29]]. However, subtle changes occur in the positions of the diffuse signal maxima

around the $0\bar{1}1$ peak, with a gradual change in their position starting below 100 K. These changes are summarized in the Supplemental Material for a $(PTO_8|STO_5)_{18}$, $(PTO_{13}|STO_5)_{12}$, and $(PTO_{16}|STO_5)_{11}$ superlattice (see Supplemental Material Figs. 7 and 8 with associated discussion).

Our experimental observations indicate that for all temperatures, the absence of diffuse scattering at $L = 0$ rules out a structure with periodic Bloch components in our $PbTiO_3/SrTiO_3$ superlattices, consistent with both second-principles and phase-field calculations for systems with domain periods larger than 14 unit cells. However, our results still leave open the possibility of a disordered Bloch structure with a random direction of the Bloch polarization, due to a lack of macroscopic coherence of the Bloch component in three dimensions. Naively, this would agree with the simulations in $PbTiO_3$ and two-dimensional $PbTiO_3/SrTiO_3$ supercells when a Bloch component is present, which show that there is no significant difference between configurations with parallel and antiparallel Bloch polarizations in adjacent walls (percentage difference in energy of $3 \times 10^{-7}\%$). Nevertheless, we note that such a small difference in energy does not necessarily exclude all macroscopic correlations: labyrinthine domain structures similar to the one in Fig. 3(a) can be created using one long meandering domain wall, and the macroscopic coherence of the Bloch component in such cases will not depend on the direct coupling between adjacent walls, but on the coherence of the Bloch component along the wall itself. Completely disordered Bloch polarization is also not consistent with recent observations of macroscopic chirality in 180° domain walls interpreted as arising from macroscopically ordered Bloch components in $PbTiO_3/SrTiO_3$ superlattices [8,50,51]. The reason for the discrepancy between our investigations and such experimental works is still uncertain. The sensitivity of the Bloch component to local strain and domain period, as shown in our second-principles calculations, could be crucial for the behavior of the polarization inside the domain walls. Additionally, different sample fabrication techniques (the aforementioned works have studied samples fabricated using pulsed laser deposition, whereas our work focuses on samples grown using off-axis sputtering), as well as the precise nature of the heterostructure (e.g., the use of a bottom $SrRuO_3$ layer), could play an important role. The reason for this discrepancy between our study and previous works therefore deserves more attention and should be investigated further in future studies.

Finally, our x-ray diffraction measurements indicate that for small, nonzero values of Q_z we detect an in-plane modulation of the atomic displacements occurring in a perpendicular direction to the 180° domain wall plane. The results are consistent with calculated diffuse scattering in the $hk1$ plane [Figs. 4(b) and 4(d)]. This diffuse scattering is a signature of the rotation of the atomic displacements at the 180° domain walls of $PbTiO_3$ driven by the depolarizing field. Our measurements therefore show that signatures of such atomic displacements can be observed in diffuse x-ray scattering, providing a macroscopic technique that can be used to study the rotation of spontaneous polarization.

VI. CONCLUSIONS

To conclude, this work focused on understanding the structure of ferroelectric domain walls in $PbTiO_3$ using a combination of first- and second-principles calculations, phase-field simulations, diffuse scattering calculations, and synchrotron-based diffuse x-ray scattering measurements. Our first- and second-principles calculations confirmed that a Bloch domain wall configuration is expected in bulk $PbTiO_3$ when strained on $SrTiO_3$, with a sizable polarization and a characteristic transition temperature of approximately 150 K. The structure of this Bloch wall is characterized by correlated displacements of the Pb cations in the direction of the Bloch polarization. On the other hand, second-principles calculations showed that the Bloch polarization in $PbTiO_3/SrTiO_3$ superlattices is extremely sensitive to the domain period and the imposed epitaxial strain and could disappear at their equilibrium domain periods.

Using the structural signature of the Bloch polarization, we calculated diffuse x-ray scattering from phase-field patterns with periodic non-Ising domain walls, with our phase-field simulations suggesting that the characteristic diffuse scattering patterns around peaks with zero out-of-plane (Q_z) components of the scattering vector would allow us to distinguish between different types of domain walls. We performed diffuse x-ray scattering measurements, and by measuring diffuse signal around low Q_z peaks in $PbTiO_3/SrTiO_3$ superlattices, we found anisotropic diffuse intensity. Diffuse scattering fingerprints of phase-field simulated patterns showed that this anisotropic diffuse intensity arises due to the ferroelectric polarization configuration associated with the flux-closure structure of the 180° domain walls, characterized by a rotation of polarization, a result of the inhomogeneous depolarizing fields in the $PbTiO_3$ layers. We observed no signature of Bloch components down to 2.2 K, consistent with our second-principles calculations.

Although our measurements do not exclude the presence of the Bloch polarization at the domain walls of all $PbTiO_3$ films and multilayers, they emphasize the importance of the boundary conditions imposed on these systems, as well as the effect of epitaxial strain and layer thickness. The simulations and measurements in this work therefore provide new insight into the structure of ferroelectric domain walls in $PbTiO_3$-based multilayers. Our work shows that the Bloch component is not ubiquitous in $PbTiO_3$ domain walls, and the nature of these nanoscale objects is intricately linked to the precise structure of the

studied films and multilayers. Our results emphasizing this sensitivity of the Bloch component hopefully reconcile contrasting observations of the nature of the domain walls of $PbTiO_3$-based thin films and multilayers found in the literature. Finally, we expect that our general guidelines for distinguishing between different types of ordered polarization configurations in ferroelectric multilayers using diffuse x-ray scattering will be useful for determining the nature of domain walls in other systems and hope they will inspire future studies.

VII. METHODS

A. First- and second-principles calculations

Our DFT calculations are performed relying on the PBEsol [52,53] exchange correlation functional as implemented in the ABINIT software [54]. The plane-wave energy cutoff was 65 Ha and the k-point grid was $8 \times 8 \times 8$ for the training set used to fit the second-principles model and was $8 \times 8 \times 1$ for the relaxation of the 60-atom cell. All structures were fully relaxed until the forces on the atoms were less than 10^{-5} Ha/bohr and the stresses were less than 10^{-7} Ha/bohr^3.

Our second-principles atomistic models of $PbTiO_3$ and $SrTiO_3$ have been constructed within the MULTIBINIT package and fitted on DFT data. The molecular dynamics (MD) calculations have been performed by using a hybrid Monte Carlo simulation within a $20 \times 12 \times 12$ supercell of the 5 atom unit cell of $PbTiO_3$. For each temperature, we performed 200 000 MD steps. Between each MD step, 40 Monte Carlo steps were performed in order to speed up the convergence and the energy landscape sampling. The local polarization has been calculated with the Born effective charge by averaging the displacements within the unit cell centered on the Pb atom following the procedure in Ref. [20].

Our second-principles model for $PbTiO_3/SrTiO_3$ superlattices has been constructed following the scheme proposed in Ref. [28]. The reference lattice parameters for $PbTiO_3/SrTiO_3$ superlattices are calculated by minimizing the elastic energy of the $SrTiO_3$ and $PbTiO_3$:

$$E = \frac{C_{\mathrm{STO}}}{2}\left(\frac{a_{\mathrm{av}} - a_{\mathrm{STO}}}{a_{\mathrm{STO}}}\right)^2 + \frac{C_{\mathrm{PTO}}}{2}\left(\frac{a_{\mathrm{av}} - a_{\mathrm{PTO}}}{a_{\mathrm{PTO}}}\right)^2,$$

where C_{STO} (C_{PTO}) are the harmonic elastic constants of $SrTiO_3$ ($PbTiO_3$) and a_{STO} (a_{PTO}) are the lattice parameters of cubic $SrTiO_3$ ($PbTiO_3$). After minimization, the a_{av} can be calculated as

$$a_{\mathrm{av}} = a_{\mathrm{STO}} a_{\mathrm{PTO}}\left(\frac{m a_{\mathrm{STO}} + a_{\mathrm{PTO}}}{m a^2{}_{\mathrm{STO}} + a^2{}_{\mathrm{PTO}}}\right), \quad \text{with } m = \frac{C_{\mathrm{STO}}}{C_{\mathrm{PTO}}}.$$

All structures were relaxed in order to minimize the force to 2×10^{-5} Ha/bohr and the stresses which were not constrained by epitaxial strain to be less than 2×10^{-7} Ha/bohr^3. In order to find the global minima of the system, we decrease the temperature from 10 to 1 K in steps of 1 K. Between each temperature we perform 2000 MD steps using hybrid Monte Carlo simulation: between each MD step, 40 Monte Carlo steps were performed.

B. Phase-field simulations

Phase-field simulations of $PbTiO_3$-based superlattices were carried out using the program FERRODO [55,56], which allows us to find stationary domain structure configurations in perovskite ferroelectrics defined by the generalized Ginzburg-Landau-Devonshire model [57]. In the spirit of the established Ginzburg-Landau-Devonshire approach to ferroelectric perovskites, the primary order-parameter field is the electric polarization $\boldsymbol{P}(\boldsymbol{R})$, which is subject to both anharmonic local interactions and long-range dipole-dipole interactions screened by an isotropic background permittivity. Furthermore, the Ginzburg-Landau-Devonshire energy functional contains terms linear or quadratic in the strain degrees of freedom. These secondary order parameters can be represented by the spatially inhomogeneous strain tensor field or the field of acoustic displacements $\boldsymbol{u}(\boldsymbol{R})$. Using the mechanical equilibrium conditions, the energy contributions containing strain degrees of freedom can be formally expressed as a function of the polarization field $\boldsymbol{P}(\boldsymbol{R})$ with the average strain as a parameter. This formal solution is used to eliminate the secondary order parameters from the model so that the renormalized Ginzburg-Landau free-energy functional with the accordingly corrected coefficients and with the additional long-range interaction term depends on the primary order parameter only. The renormalization is implicit in the tabulated Ginzburg-Landau model parameters so that, technically, the renormalization consists in adding the long-range fields only. The temporal evolution $\boldsymbol{P}(\boldsymbol{R})$ toward energy optimum is searched numerically by solving the time-dependent Ginzburg-Landau equation for such renormalized Ginzburg-Landau free energy.

The phase-field simulations were performed on a simulation box of $216 \times 216 \times 216$ sites consisting of 12 superlattice periods along the z axis, each with 13 sites of $PbTiO_3$ and 5 sites of $SrTiO_3$. The spatial step was 0.4 nm. The domain structure in the main text was relaxed following 300 000 iterations from a white noise initial condition under periodic boundary conditions and epitaxial clamping conditions imposing the average in-plane strain ($e_{xx} = -0.015$, $e_{yy} = -0.015$, $e_{xy} = 0$), with the former values estimated from the mismatch between the experimental lattice parameter of $SrTiO_3$ and hypothetic cubic $PbTiO_3$ crystal at ambient conditions [58]. Ferroelectric $PbTiO_3$ was described by the same model as in Ref. [59] applied to study $PbTiO_3$-paraelectric superlattices. The Landau parameters at 298 K are $\alpha_1 = -1.709 \times 10^8$ Jm C^{-2}, $\alpha_{11} = -7.25 \times 10^7$ Jm^5 C^{-4},

$\alpha_{12} = 7.5 \times 10^8$ Jm^5 C^{-4}, $\alpha_{111} = 2.61 \times 10^8$ Jm^9 C^{-6}, $\alpha_{112} = 6.1 \times 10^8$ Jm^9 C^{-6}, $\alpha_{123} = -3.66 \times 10^9$ Jm^9 C^{-6}, with gradient parameters $G_{11} = 1 \times 10^{-10}$ Jm^3 C^{-2}, $G_{12} = -1 \times 10^{-10}$ Jm^3 C^{-2}, $G_{44} = 1 \times 10^{-10}$ Jm^3 C^{-2}, elastic components $C_{11} = 1.746 \times 10^{11}$ Jm^{-3}, $C_{12} = 7.94 \times 10^{10}$ Jm^{-3}, $C_{44} = 1.111 \times 10^{11}$ Jm^{-3}, and electrostriction parameters $q_{11} = 1.1412 \times 10^{10}$ Jm C^{-2}, $q_{12} = 4.6 \times 10^8$ Jm C^{-2}, $q_{44} = 7.5 \times 10^9$ Jm C^{-2}, $Q_{11} = 0.089$ m^4 C^{-2}, $Q_{12} = -0.026$ m^4 C^{-2}, $Q_{44} = 0.0675$ m^4 C^{-2}. The background permittivity ε_B, as defined in Refs. [57,59], was set to 1. The Landau parameters of paraelectric $SrTiO_3$ were set as in Ref. [60] ($\alpha_1 = 1.829 \times 10^8$ Jm C^{-2}, $\alpha_{11} = 1.696 \times 10^9$ Jm^5 C^{-4}, $\alpha_{12} = 3.918 \times 10^8$ Jm^5 C^{-4} at 298 K), and the gradient, elastic, electrostriction, and electrostatic terms were kept the same as its ferroelectric counterpart. The values of the dimensionless soft mode eigenvector ($d_{Pb} = 0.0194$, $d_{Ti} = -0.0163$, $d_{O1} = d_{O2} = d_{O3} = -0.0802$) and of the effective flexoelectric tensor ($f_{11} = -6.1$ V, $f_{12} = -2.8$ V, $f_{44} = 2f_{1212} = -3.9$ V) have been determined using the second-principles model for $PbTiO_3$ described in this work. The values were adjusted to best match with the corresponding correlations between the atomic displacements and polarization within a representative auxiliary multidomain configuration generated by incomplete annealing of a $4 \times 12 \times 20$ $PbTiO_3$ supercell of initially disordered displacements.

C. Diffuse scattering calculations

To calculate the diffuse scattering maps, the crystal structure was generated from the relaxed polarization field $\boldsymbol{P}(\boldsymbol{R})$ by considering two contributions: local polar distortions $\boldsymbol{p_a}(\boldsymbol{R})$ and local acoustic displacements $\boldsymbol{u}(\boldsymbol{R})$. Local polar distortions $\boldsymbol{p_a}(\boldsymbol{R})$ were expected to be directly proportional to the polarization field $\boldsymbol{P}(\boldsymbol{R})$. The conversion of the local polarization $\boldsymbol{P}(\boldsymbol{R})$ at the lattice vector $\boldsymbol{R}$ to the atomic displacements within the corresponding perovskite unit cell was achieved using a linear relationship: $\boldsymbol{p}_a(\boldsymbol{R}) = d_a \boldsymbol{P}(\boldsymbol{R})(a_0/|P_s|)$. Here, $a_0 = 0.4$ nm is a reference lattice constant, $P_s = 0.755$ C/m^2 is the spontaneous polarization of monodomain $PbTiO_3$ at 298 K (as it appears in phenomenological Landau models), the index a runs through the 5 atomic sublattices of the ABO_3 perovskite structure, and d_a form dimensionless components of the soft mode eigenvector attached to the polarization in the Landau potential. The acoustic displacements $\boldsymbol{u}(\boldsymbol{R})$ were calculated from the polarization field assuming mechanical equilibrium conditions with the help of the elastostatic Green function method [61] considering electrostriction and flexoelectric coupling to the polarization. The strain components ε_{ij} were evaluated from displacements $\boldsymbol{u}$ via $\varepsilon_{ij} = \frac{1}{2}[(du_i/dx_j) + (du_j/dx_i)]$, where $i, j = 1, 2, 3$. Both contributions to atomic displacements were used to generate an A-centered perovskite structure with the reference lattice constant 0.4 nm, which was used as an input to the MP_TOOLS software package [62] to calculate x-ray scattering maps. Diffuse scattering data were symmetrized by considering the overall 4*mm* symmetry.

D. Sample growth

$PbTiO_3/SrTiO_3$ superlattices were deposited on TiO_2-terminated (001) $SrTiO_3$ substrates (Crystec GmbH) using off-axis radio frequency (rf) magnetron sputtering. The $PbTiO_3$ and $SrTiO_3$ layers were deposited from $Pb_{1.1}TiO_3$ and $SrTiO_3$ ceramic targets, respectively, in a 0.18 Torr atmosphere with an oxygen to argon flow ratio of 20.4/28.7 and rf power of 60 W. During growth, the substrate was kept at a constant temperature of 560 °C, as measured by a thermocouple inside the heating block.

E. Diffuse x-ray scattering measurements

Diffuse x-ray scattering measurements were performed at the ID28 beamline (ESRF, France) in grazing incidence reflection geometry with incident photon wavelength $\lambda = 0.98$ Å [63]. All measurements were performed with the film rotated 45° perpendicular to the beam, minimizing the impact of the excluded cone. Data were treated using the CrysAlis Pro software package (Rigaku Oxford Diffraction) and high-resolution reciprocal space reconstructions were produced using in-house beamline software. No symmetry averaging or space filling routines were applied. All measurements were conducted at room temperature.

F. High-resolution synchrotron x-ray diffraction measurements

High-resolution synchrotron x-ray diffraction measurements were performed at beamline ID01 at ESRF [64], using an incoherent x-ray beam (approximately 50×50 μm^2 full width at half maximum) to probe the average domain behavior. An incident x-ray energy of 9 keV was selected using a Si (111) double crystal monochromator. High-temperature measurements were performed with the sample mounted on a resistive heater using a high-temperature ceramic adhesive. Low-temperature measurements were performed by mounting the samples on a custom continuous flow liquid He cryostat. The samples were mounted on an aluminum stage using General Electric (GE) varnish. The temperature of the samples was monitored using a Cernox thermometer and controlled using a cartridge resistor (50 Ω, 25 W), both connected to a Lakeshore 340 temperature controller.

The data that support the findings of this study are openly available in the Yareta repository [65]. The obtained raw data from the ID01 experiments can be accessed from the ESRF data portal from March 2025 at [66] and [67]. Further data are available from the authors upon reasonable request.

ACKNOWLEDGMENTS

The authors thank Evgenios Stylianidis for help with sample fabrication, Pavel Márton for help with treating second-principles data, Jiří Kulda for his generous support with the MP_TOOLS software package, and Jorge Íñiguez-González and Fernando Gómez-Ortiz for fruitful discussions. This work was supported by the Swiss National Science Foundation (SNSF) Scientific Exchanges Scheme [Grant No. IZSEZ0_212990 (M.H.)], by Division II of the SNSF [Project No. 200021_200636 (C.L., L. T., J.-M.T., M.H.)], and the European Union's Horizon 2020 research and innovation program [Grant Agreement No. 766726—TSAR (P.O., L. B., A. S., P. Z., P. G., J.H.)]. P. O. and J. H. acknowledge the assistance provided by the Operational Programme Johannes Amos Comenius of the Ministry of Education, Youth and Sport of the Czech Republic, within the frame of project Ferroic Multifunctionalities (FerrMion) [Project No. CZ.02.01.01/00/22_008/0004591], co-funded by the European Union. P. G. acknowledges support from F.R.S.-FNRS Belgium (Grant No. T.0107.20, PROMOSPAN). M. H. acknowledges support from UK Research and Innovation (UKRI). We acknowledge the European Synchrotron Radiation Facility for provision of synchrotron radiation facilities and the ID01 and ID28 beamline staff for support during the synchrotron experiments. For simulations, we acknowledge access to the CECI supercomputer facilities funded by the F.R.S.-FNRS Belgium (Grant No. 2.5020.1) and to the Tier-1 supercomputer of the Fédération Wallonie-Bruxelles funded by the Walloon Region of Belgium (Grant No. 1117545).

[1] G. Catalan, J. Seidel, R. Ramesh, and J. F. Scott, *Domain wall nanoelectronics*, Rev. Mod. Phys. **84**, 119 (2012).

[2] I. I. Naumov, L. Bellaiche, and H. Fu, *Unusual phase transitions in ferroelectric nanodisks and nanorods*, Nature (London) **432**, 737 (2004).

[3] P. Aguado-Puente and J. Junquera, *Ferromagneticlike closure domains in ferroelectric ultrathin films: First-principles simulations*, Phys. Rev. Lett. **100**, 177601 (2008).

[4] C. T. Nelson *et al.*, *Spontaneous vortex nanodomain arrays at ferroelectric heterointerfaces*, Nano Lett. **11**, 828 (2011).

[5] C.-L. Jia, K. W. Urban, M. Alexe, D. Hesse, and I. Vrejoiu, *Direct observation of continuous electric dipole rotation in flux-closure domains in ferroelectric* $Pb(Zr,Ti)O_3$, Science **331**, 1420 (2011).

[6] Y. L. Tang *et al.*, *Observation of a periodic array of flux-closure quadrants in strained ferroelectric* $PbTiO_3$ *films*, Science **348**, 547 (2015).

[7] A. K. Yadav *et al.*, *Observation of polar vortices in oxide superlattices*, Nature (London) **530**, 198 (2016).

[8] S. Das *et al.*, *Observation of room-temperature polar skyrmions*, Nature (London) **568**, 368 (2019).

[9] Y. J. Wang *et al.*, *Polar meron lattice in strained oxide ferroelectrics*, Nat. Mater. **19**, 881 (2020).

[10] D. Rusu *et al.*, *Ferroelectric incommensurate spin crystals*, Nature (London) **602**, 240 (2022).

[11] D. Lee, R. K. Behera, P. Wu, H. Xu, Y. L. Li, S. B. Sinnott, S. R. Phillpot, L. Q. Chen, and V. Gopalan, *Mixed Bloch-Néel-Ising character of 180° ferroelectric domain walls*, Phys. Rev. B **80**, 060102(R) (2009).

[12] P. Marton, I. Rychetsky, and J. Hlinka, *Domain walls of ferroelectric* $BaTiO_3$ *within the Ginzburg-Landau-Devonshire phenomenological model*, Phys. Rev. B **81**, 144125 (2010).

[13] J. C. Wojdeł and J. Íñiguez, *Ferroelectric transitions at ferroelectric domain walls found from first principles*, Phys. Rev. Lett. **112**, 247603 (2014).

[14] S. Cherifi-Hertel, H. Bulou, R. Hertel, G. Taupier, K. D. Dorkenoo, C. Andreas, J. Guyonnet, I. Gaponenko, K. Gallo, and P. Paruch, *Non-Ising and chiral ferroelectric domain walls revealed by nonlinear optical microscopy*, Nat. Commun. **8**, 15768 (2017).

[15] C. Weymann, S. Cherifi-Hertel, C. Lichtensteiger, I. Gaponenko, K. D. Dorkenoo, A. B. Naden, and P. Paruch, *Non-Ising domain walls in c-phase ferroelectric lead titanate thin films*, Phys. Rev. B **106**, L241404 (2022).

[16] Y.-J. Wang, Y.-L. Zhu, and X.-L. Ma, *Chiral phase transition at 180° domain walls in ferroelectric* $PbTiO_3$ *driven by epitaxial compressive strains*, J. Appl. Phys. **122**, 134104 (2017).

[17] F. Gómez-Ortiz, P. García-Fernández, J. M. López, and J. Junquera, *Melting of crystals of polarization vortices and chiral phase transitions in oxide superlattices*, Phys. Rev. B **105**, L220103 (2022).

[18] R. Wahl, D. Vogtenhuber, and G. Kresse, $SrTiO_3$ *and* $BaTiO_3$ *revisited using the projector augmented wave method: Performance of hybrid and semilocal functionals*, Phys. Rev. B **78**, 104116 (2008).

[19] J. C. Wojdeł, P. Hermet, M. P. Ljungberg, P. Ghosez, and J. Íñiguez, *First-principles model potentials for lattice-dynamical studies: General methodology and example of application to ferroic perovskite oxides*, J. Phys. Condens. Matter **25**, 305401 (2013).

[20] B. Meyer and D. Vanderbilt, *Ab initio study of ferroelectric domain walls in* $PbTiO_3$, Phys. Rev. B **65**, 104111 (2002).

[21] P. Aguado-Puente and J. Junquera, *Structural and energetic properties of domains in* $PbTiO_3/SrTiO_3$ *superlattices from first principles*, Phys. Rev. B **85**, 184105 (2012).

[22] B. C. Frazer, H. R. Danner, and R. Pepinsky, *Single-crystal neutron analysis of tetragonal* $BaTiO_3$, Phys. Rev. **100**, 745 (1955).

[23] G. H. Kwei, A. C. Lawson, S. J. L. Billinge, and S. W. Cheong, *Structures of the ferroelectric phases of barium titanate*, J. Phys. Chem. **97**, 2368 (1993).

[24] G. Shirane, R. Pepinsky, and B. C. Frazer, *X-ray and neutron diffraction study of ferroelectric* $PbTiO_3$, Acta Crystallogr. **9**, 131 (1956).

[25] F. Gómez-Ortiz, H. Aramberri, J. M. López, P. García-Fernández, J. Íñiguez, and J. Junquera, *Kittel law and domain formation mechanism in* $PbTiO_3/SrTiO_3$ *superlattices*, Phys. Rev. B **107**, 174102 (2023).

[26] J. S. Baker and D. R. Bowler, *Polar morphologies from first Principles:* $PbTiO_3$ *films on* $SrTiO_3$ *substrates and the* $p(2 \times \Lambda)$ *surface reconstruction*, Adv. Theory Simulations **3**, 2000154 (2020).

[27] J. Wu, J. Yang, L. Ma, L. Zhang, and S. Liu, *Modular development of deep potential for complex solid solutions*, Phys. Rev. B **107**, 144102 (2023).

[28] C. Escorihuela Sayalero, *Second-principles methods for large-scale simulations of realistic functional oxides*, Ph.d. Thesis, University of Luxembourg, 2019.

[29] See Supplemental Material at http://link.aps.org/supplemental/10.1103/PhysRevX.14.041052 for the extraction of the superlattice equilibrium domain period from second-principles calculations, schematics of the expected diffraction patterns for different types of domain walls, the comparison of diffuse scattering from superlattices with different layer thicknesses, a discussion on the asymmetry of the scattering near the $L = 1$ substrate peak, a comparison of the 1054 and 101 superlattice peaks, and a discussion of the high-resolution measurements at low and high temperatures.

[30] G. Catalan, A. Lubk, A. H. G. Vlooswijk, E. Snoeck, C. Magen, A. Janssens, G. Rispens, G. Rijnders, D. H. A. Blank, and B. Noheda, *Flexoelectric rotation of polarization in ferroelectric thin films*, Nat. Mater. **10**, 963 (2011).

[31] F. H. Gong *et al.*, *Atomic mapping of periodic dipole waves in ferroelectric oxide*, Sci. Adv. **7**, eabg5503 (2021).

[32] S. K. Streiffer, J. A. Eastman, D. D. Fong, C. Thompson, A. Munkholm, M. V. Ramana Murty, O. Auciello, G. R. Bai, and G. B. Stephenson, *Observation of nanoscale 180° stripe domains in ferroelectric* $PbTiO_3$ *thin films*, Phys. Rev. Lett. **89**, 067601 (2002).

[33] D. D. Fong, G. B. Stephenson, S. K. Streiffer, J. A. Eastman, O. Auciello, P. H. Fuoss, and C. Thompson, *Ferroelectricity in ultrathin perovskite films*, Science **304**, 1650 (2004).

[34] C. Thompson, D. D. Fong, R. V. Wang, F. Jiang, S. K. Streiffer, K. Latifi, J. A. Eastman, P. H. Fuoss, and G. B. Stephenson, *Imaging and alignment of nanoscale 180° stripe domains in ferroelectric thin films*, Appl. Phys. Lett. **93**, 182901 (2008).

[35] C. Lichtensteiger, S. Fernandez-Pena, C. Weymann, P. Zubko, and J. M. Triscone, *Tuning of the depolarization field and nanodomain structure in ferroelectric thin films*, Nano Lett. **14**, 4205 (2014).

[36] M. Hadjimichael, E. Zatterin, S. Fernandez-Peña, S. J. Leake, and P. Zubko, *Domain wall orientations in ferroelectric superlattices probed with synchrotron x-ray diffraction*, Phys. Rev. Lett. **120**, 037602 (2018).

[37] M. Seul and D. Andelman, *Domain shapes and patterns: The phenomenology of modulated phases*, Science **267**, 476 (1995).

[38] P. Zubko, N. Jecklin, A. Torres-Pardo, P. Aguado-Puente, A. Gloter, C. Lichtensteiger, J. Junquera, O. Stéphan, and J.-M. M. Triscone, *Electrostatic coupling and local structural distortions at interfaces in ferroelectric/paraelectric superlattices*, Nano Lett. **12**, 2846 (2012).

[39] S. L. Zhang, G. Van Der Laan, and T. Hesjedal, *Direct experimental determination of the topological winding number of skyrmions in* Cu_2OSeO_3, Nat. Commun. **8**, 14619 (2017).

[40] J. Y. Chauleau, W. Legrand, N. Reyren, D. Maccariello, S. Collin, H. Popescu, K. Bouzehouane, V. Cros, N. Jaouen, and A. Fert, *Chirality in magnetic multilayers probed by the symmetry and the amplitude of dichroism in x-ray resonant magnetic scattering*, Phys. Rev. Lett. **120**, 037202 (2018).

[41] S. L. Zhang, G. van der Laan, W. W. Wang, A. A. Haghighirad, and T. Hesjedal, *Direct observation of twisted surface skyrmions in bulk crystals*, Phys. Rev. Lett. **120**, 227202 (2018).

[42] S. Zhang, G. Van Der Laan, J. Müller, L. Heinen, M. Garst, A. Bauer, H. Berger, C. Pfleiderer, and T. Hesjedal, *Reciprocal space tomography of 3D skyrmion lattice order in a chiral magnet*, Proc. Natl. Acad. Sci. U.S.A. **115**, 6386 (2018).

[43] W. Li *et al.*, *Anatomy of skyrmionic textures in magnetic multilayers*, Adv. Mater. **31**, 1807683 (2019).

[44] E. Bousquet, M. Dawber, N. Stucki, C. Lichtensteiger, P. Hermet, S. Gariglio, J.-M. Triscone, and P. Ghosez, *Improper ferroelectricity in perovskite oxide artificial superlattices*, Nature (London) **452**, 732 (2008).

[45] J. Bang, N. Strkalj, M. Sarott, M. Trassin, and T. Weber, *Probing hidden order in ferroelectric oxide thin films with single-crystal diffuse x-ray scattering*, Acta Crystallogr. Sect. A **78**, e577 (2022).

[46] K. Huang, *X-ray reflexions from dilute solid solutions*, Proc. R. Soc. A. **190**, 102 (1947).

[47] P. H. Dederichs, *The theory of diffuse x-ray scattering and its application to the study of point defects and their clusters*, J. Phys. F **3**, 471 (1973).

[48] B. J. Campbell, S. K. Sinha, R. Osborn, S. Rosenkranz, J. F. Mitchell, D. N. Argyriou, L. Vasiliu-Doloc, O. H. Seeck, and J. W. Lynn, *Polaronic orbital polarization in a layered colossal magnetoresistive manganite*, Phys. Rev. B **67**, 020409(R) (2003).

[49] J. Y. Jo, P. Chen, R. J. Sichel, S. J. Callori, J. Sinsheimer, E. M. Dufresne, M. Dawber, and P. G. Evans, *Nanosecond dynamics of ferroelectric/dielectric superlattices*, Phys. Rev. Lett. **107**, 055501 (2011).

[50] M. R. McCarter *et al.*, *Structural chirality of polar skyrmions probed by resonant elastic x-ray scattering*, Phys. Rev. Lett. **129**, 247601 (2022).

[51] Y.-T. Shao *et al.*, *Emergent chirality in a polar meron to skyrmion phase transition*, Nat. Commun. **14**, 1355 (2023).

[52] D. R. Hamann, *Optimized norm-conserving Vanderbilt pseudopotentials*, Phys. Rev. B **88**, 085117 (2013).

[53] M. J. van Setten, M. Giantomassi, E. Bousquet, M. J. Verstraete, D. R. Hamann, X. Gonze, and G. M. Rignanese, *The PSEUDODOJO: Training and grading a 85 element optimized norm-conserving pseudopotential table*, Comput. Phys. Commun. **226**, 39 (2018).

[54] X. Gonze *et al.*, *The ABINIT project: Impact, environment and recent developments*, Comput. Phys. Commun. **248**, 107042 (2020).

[55] P. Marton and J. Hlinka, *Simulation of domain patterns in* $BaTiO_3$, Phase Transitions **79**, 467 (2006).

[56] J. Hlinka and P. Márton, *Phenomenological model of a 90° domain wall in* $BaTiO_3$*-type ferroelectrics*, Phys. Rev. B **74**, 104104 (2006).

[57] P. Ondrejkovic, P. Marton, V. Stepkova, and J. Hlinka, *Fundamental properties of ferroelectric domain walls from Ginzburg–Landau models*, in *Domain Walls: From Fundamental Properties to Nanotechnology*, edited by D. Meier, J. Seidel, M. Gregg, and R. Ramesh (Oxford University Press, New York, 2020), pp. 76–108.

[58] V. G. Koukhar, N. A. Pertsev, and R. Waser, *Thermodynamic theory of epitaxial ferroelectric thin films with dense domain structures*, Phys. Rev. B **64**, 214103 (2001).

[59] M. Hadjimichael *et al.*, *Metal–ferroelectric supercrystals with periodically curved metallic layers*, Nat. Mater. **20**, 495 (2021).

[60] G. Sheng, Y. L. Li, J. X. Zhang, S. Choudhury, Q. X. Jia, V. Gopalan, D. G. Schlom, Z. K. Liu, and L. Q. Chen, *A modified Landau–Devonshire thermodynamic potential for strontium titanate*, Appl. Phys. Lett. **96**, 232902 (2010).

[61] J. Hlinka and E. Klotins, *Application of elastostatic Green function tensor technique to electrostriction in cubic, hexagonal and orthorhombic crystals*, J. Phys. Condens. Matter **15**, 5755 (2003).

[62] J. Kulda, *MP_TOOLS: Neutron and x-ray diffuse scattering from distorted lattices*, https://mptools.fr.

[63] A. Girard, T. Nguyen-Thanh, S. M. Souliou, M. Stekiel, W. Morgenroth, L. Paolasini, A. Minelli, D. Gambetti, B. Winkler, and A. Bosak, *A new diffractometer for diffuse scattering studies on the ID28 beamline at the ESRF*, J. Synchrotron Radiat. **26**, 272 (2019).

[64] S. J. Leake *et al.*, *The nanodiffraction beamline ID01/ESRF: A microscope for imaging strain and structure*, J. Synchrotron Radiat. **26**, 571 (2019).

[65] 10.26037/yareta:rt7uwof32jhdxbs54h7qhx4q5a

[66] C. Lichtensteiger, E. Zatterin, M. Hadjimichael, and S. Leake, *Probing phase transitions in ferroelectric domain walls with x-ray diffraction*, European Synchrotron Radiation Facility, 2024, 10.15151/ESRF-ES-550197419.

[67] C. Lichtensteiger, E. Zatterin, Ludovica Tovaglieri, M. Hadjimichael, and S. Leake, *Probing phase transitions in ferroelectric domain walls with x-ray diffraction*, European Synchrotron Radiation Facility, 2025, 10.15151/ESRF-ES-649493071.